Article:
Hooper, T.E., Crick, A., Killeen, J.H. et al. (1 more author) (2024) Structural and dielectric properties of CaSnO3-doped Sr2.1Na0.8Nb5O15 ceramics. Journal of the European Ceramic Society, 44 (12). pp. 6960-6966. ISSN 0955-2219

https://doi.org/10.1016/j.jeurceramsoc.2024.04.047

Structural and Dielectric Properties of $CaSnO_3$-doped $Sr_{2.1}Na_{0.8}Nb_5O_{15}$ Ceramics

Thomas E. Hooper[1], Alexander Crick, James H. Killeen, and Derek C. Sinclair

Department of Materials Science and Engineering, Sir Robert Hadfield Building, University of Sheffield, Mappin Street, Sheffield S1 3JD, UK

Abstract. *The crystallographic, microstructural, and dielectric properties of $Sr_{2.1}Na_{0.8-x}Ca_xNb_{5-x}Sn_xO_{15}$ (x = 0.00, 0.01, 0.05, 0.10) polycrystalline ceramics have been studied by X-ray diffraction (XRD), scanning electron microscopy (SEM), dielectric spectroscopy (DS) and impedance spectroscopy (IS). For x=0.00, 0.05, and 0.10, samples are single phase with P4bm phase at room temperature with x = 0.01 showing a small quantity of secondary phase(s). All compositions show typical ceramic microstructure and d_{50} grain sizes ranging from 5.1 to 26.6 μm. DS shows a clear trend in the high temperature ferroelectric-paraelectric transition with the Curie temperature, T_0, decreasing from ~ 160 to ~ 110 °C, and an additional relaxation at approximately 120 °C with increasing $CaSnO_3$. IS reveals all samples have a homogeneous electrical microstructure with predominantly electronic conduction. The activation energy of conduction calculated from Arrhenius plots of the conductivity increases with $CaSnO_3$ content from 1.27 to 1.38 eV likely due to the expansion of the band gap.*

Keywords: Tungsten Bronze, Ferroelectric, Dielectric, Impedance Spectroscopy, Doping

[1] Corresponding author: thomas.elliot.hooper@gmail.com

1. Introduction

Tetragonal Tungsten Bronze (TTB) ferroelectrics are materials that offer a range of versatility with regards to ionic substitution and solid solution formation [1-6]. TTBs have corner sharing oxygen octahedra which arrange themselves to form 3 distinct A-sites with 15-, 12- and 9-fold coordination as shown in Figure 1. TTBs can be divided into three categories: 'stuffed' where all A1, A2 and C-sites are occupied, eg. $K_6Li_4Nb_{10}O_{30}$ [7, 8]; 'filled' where A1 and A2 sites are fully occupied and C-sites are unoccupied, eg. $Sr_5LaTi_3Nb_7O_{30}$ [9]; and 'unfilled' where A1 and A2 occupancy is <100% and C-sites are unoccupied, eg. $(Sr,Ba)_5Nb_{10}O_{30}$ [6, 10-12].

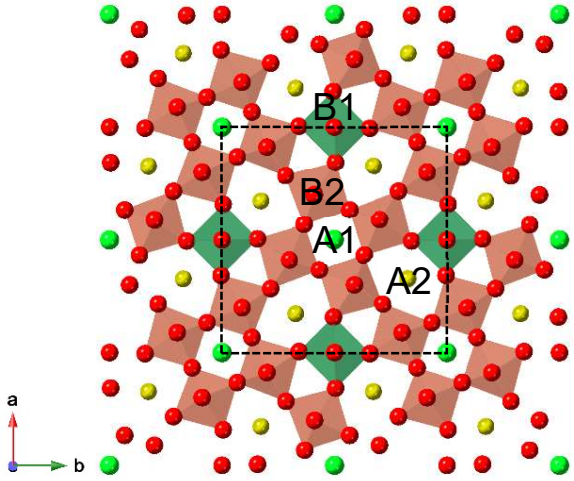

Figure 1 (single column width): Crystal structure of $Sr_2NaNb_5O_{15}$ tungsten bronze structure generated in CrystalMaker according to ICDD #04-006-4820. The dashed box represents the unit cell according to *P*4*bm* symmetry.

Strontium sodium niobate ($Sr_2NaNb_5O_{15}$ hereby referred to as SNN) complies with the aristotype TTB structure $(A1)_2(A2)_4(C1)_4(B1)_8(B2)_2O_{30}$ with Nb^{5+} ions located on B1- and B2-sites, and Sr^{2+} and Na^+ ions distributed on both the A1 and A2-sites owing to their similar ionic radii [13, 14]. The C-site is assumed to remain empty due to the inability to accommodate larger ions, although it is not clear what the upper and lower bounds for occupying this site are yet. According to the $NaNbO_3$ – $SrNb_2O_6$ phase diagram proposed by Tang *et al.* [15], the formation of single phase SNN relies on the presence of A-site vacancies and therefore must be an unfilled TTB, with filled $Sr_2NaNb_5O_{15}$ producing secondary phase $NaNbO_3$ perovskite, although this is more likely to be Sr-doped $NaNbO_3$ as proposed by Torres-Pardo *et al.* [14]. Furthermore, the conversion from a filled to an unfilled TTB has been demonstrated by the successful removal of secondary phase(s) [16, 17]. The dielectric properties of SNN are characterised by two distinct peaks labelled T1 and T2, where T2 is associated with the

ferroelectric-paraelectric phase transition occurring between 250 and 300 ºC, and T1 is associated with the smeared-out phase transition to a frustrated ferroelectric/ferroelastic low temperature state owing to changes in the elastic properties [13, 14].

Many doping studies have been carried out on SNN, however the aims and objectives of these doping studies vary depending on the proposed application. For example, doping regimes within the high energy density community aim to promote the room temperature relaxor behaviour to increase the recoverable energy density [18-21]. The dielectrics community aims to increase ionic disorder to break up long range ferroelectric transitions and improve dielectric temperature stability [22]. The piezoelectric community aim to form a morphotropic phase boundary (MPB) to create energetic degeneracy between two phases to improve domain switching capabilities and subsequent piezoelectric properties [23-27]. Most of these doping studies have related to exclusive A-site substitution for Sr^{2+}, Na^{+} and co-doping both Sr and Na [16, 20, 23, 26-34], with only a limited amount of B-site doping being carried out [35, 36]. In general, doping with isovalent ions of larger radius than that of Sr^{2+} or Na^{+} such as Ba^{2+} or K^{+} expands the unit cell along the c-axis, increasing tetragonality and stabilising the [001] polar mode. This results in a decrease and sometimes a complete disappearance of the low temperature T1 transition as the commensurate tilting that occurs to allow for the ferroelastic transition is no longer possible [31, 32, 34, 37]. Conversely, isovalent doping with smaller ions such as Ca^{2+} and rare-earth elements, increases the unit cell along the a-b plane and reduces the tetragonality. The destabilisation of the polar [001] mode results in a decrease in the magnitude of ε' at the high temperature T2 transition. The expansion of the unit cell along the a-b plane allows for a greater ease of commensurate tilting and therefore the low temperature T1 transition transforms from broad relaxor-like behaviour to a proper ferroelectric transition with little frequency dispersion [19, 23, 38, 39].

Doping studies of SNN are more focussed on the influence of single dopant or dopants, whereas there have been limited studies on the effects of forming solid solutions. Here, we aim to expand the knowledge of ternary solid solution formations with single phase $Sr_{2.1}Na_{0.8}Nb_5O_{15}$ (hereby referred to as SNN0.8) by doping with $CaSnO_3$ perovskite to 10 mol%.

2. Experimental Procedure

Commercially available reagents of $SrCO_3$ (Sigma Aldrich, 99.9%), Na_2CO_3 (Sigma Aldrich, 99.5%), $CaCO_3$ (Fisons, 99%), SnO_2 (Sigma Aldrich, 99.9 %) and Nb_2O_5 (Gemch Ltd., 99.5%) were dehydrated overnight. Appropriate reagents to synthesise $SrNb_2O_6$, $CaSnO_3$ and $NaNbO_3$ were weighed stoichiometrically, ball milled in isopropanol for 24 hours, dried and

sieved, and calcined at 1100 ºC (4h), 900 ºC (3h) and 800 ºC (5h), respectively. End members were then weighed according to Equation 1, and milled, dried, and sieved for a final time.

$$2.1SrNb_2O_6 + (0.8 - x)NaNbO_3 + (x)CaSnO_3 \rightarrow Sr_{2.1}Na_{0.8-x}Ca_xNb_{5-x}Sn_xO_{15} \quad (1)$$

Powders were uniaxially pressed at 12.5 MPa into 10 mm diameter pellets and cold isostatically pressed at 221 MPa for 1 minute. Pellets were buried in powder of the same composition and sintered at 1325-1450 ºC for 5 h.

X-ray diffraction (XRD) was performed on crushed sintered bulk samples which were annealed at 600°C for an hour before being cooled at a rate of 0.8°Cmin^{-1} to alleviate any crystallite strain imposed by grinding. Data were collected using monochromatic molybdenum $K\alpha_1$ (λ=0.7096 Å) radiation, measured using a STOE STADI P diffractometer with a Mythen detector and step size 0.015°. Rietveld refinements were conducted for the diffraction patterns using GSAS-II software [40] where refined parameters included lattice parameters, atomic coordinates, site occupancies, atomic thermal parameters, microstrain and crystallite size.

Ceramic microstructure was analysed using an Inspect F50 scanning electron microscope (FEI, Netherlands) with accelerating voltage of 20 kV and working distance of 9.8 mm. Samples were polished beforehand using diamond paste (Beuhler) from 6 to 1 µm and thermally etched at 200 ºC below the respective sintering temperature for 15 minutes before sputter coating a 5 nm Au layer to avoid charging.

For electrical measurements, samples were ground and polished using SiC paper and electroded using fire-on Au paste at 850 ºC for 2 h. High temperature Dielectric Spectroscopy (DS) and Impedance Spectroscopy (IS) analysis were carried out using an Agilent E4980A Precision LCR Meter connected to a tube furnace. IS measurements were carried out using a 0.1 V *ac* signal from 20 Hz to 1 MHz at 25 ºC intervals with 20 minutes dwell time to thermally equilibrate the sample. Subambient DS analysis was carried out using an Agilent E4980A Precision LCR Meter connected to a Cryodrive 1.5 cryocooler (Oxford Instruments, UK).

3. Results and Discussion

All sample geometric densities exceeded 92% based on theoretical densities calculated from XRD lattice parameters. It should be noted that although Li *et al*. [41] demonstrated the absence of abnormal grain growth in undoped SNN by a two-stage synthesis, here abnormal grain growth was still observed in SNN0.8 samples sintered >1340 ºC as demonstrated by the significant intragranular stresses and subsequent macro cracking (Supplementary Material Figure S1).

XRD patterns for all compositions are shown in Figure 2 and refined parameters are shown in Table 1. For x = 0.00, 0.05, and 0.10, samples show single phase materials attributed to the *P*4*bm* structure at room temperature which is analogous with some literature [21, 22, 24-26, 28, 32]. No observations of superlattice reflections attributed to orthorhombic space groups such as *Im*2*a*, *Ccm*2 or *Ama*2 can be observed as in Ref. [13, 14, 29, 35]. For x = 0.01, a small amount of secondary phase can be observed (Figure 2b) which could not be attributed to any reagents, end members, or any materials on the PDF4+ crystallographic database. It is clear from Figure 1 that the solid solution limit exceeds x = 0.10 and therefore may provide an opportunity to further explore this compositional space. Lattice parameters and unit cell volume against composition are shown in Figure 3. For single phase materials, the introduction of $CaSnO_3$ results in the expansion of the unit cell along the a-b plane and a shrinking along the [001]. Overall this results in a decrease in the unit cell volume owing to the substitution of Na^+ (1.39 Å [42]) with smaller Ca^{2+} (1.34 Å [42]) ions.

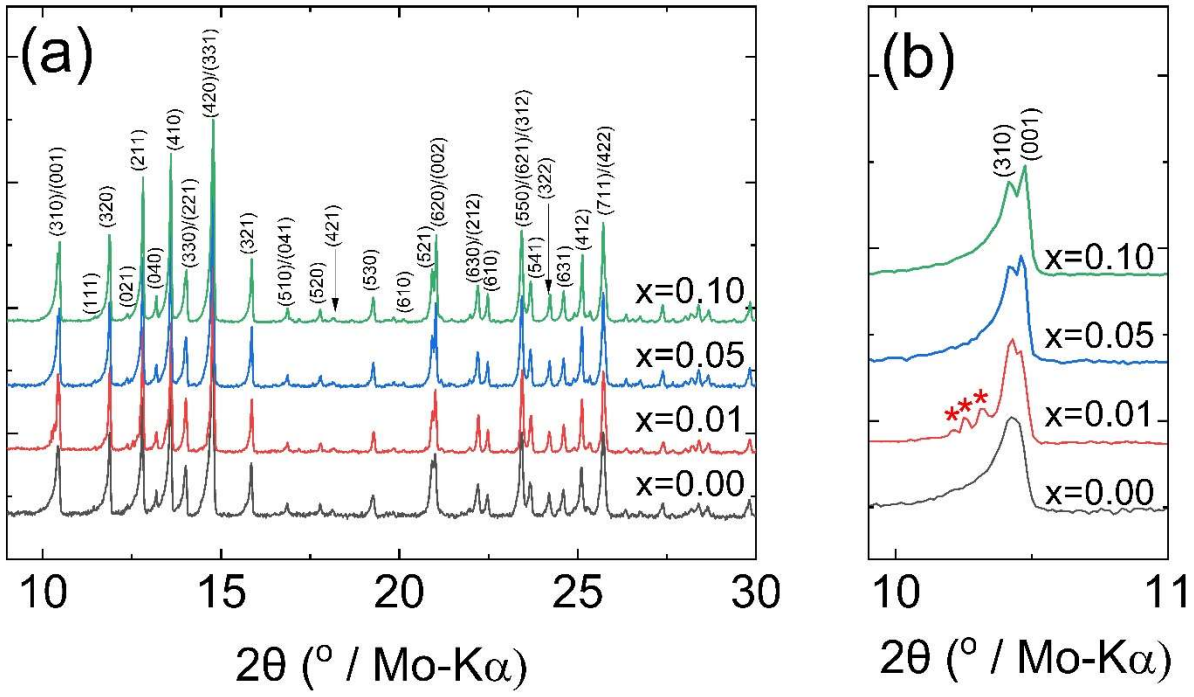

Figure 2 (2 column width): XRD Mo-Kα source scans for $Sr_{2.1}Na_{0.8-x}Ca_xNb_{5-x}Sn_xO_3$ (x = 0.00, 0.01, 0.05, and 0.10) from (a) 9° – 30° 2θ, and (b) 9.8° to 11° 2θ. Peak indexing carried out according to ICDD file with red asterisks highlighting an undetermined secondary phase. Full Rietveld refinements are provided in Figure S1 in the Supplementary Material.

Table 1: Unit cell parameters indexed using a P4bm structure for $Sr_{2.1}Na_{0.8-x}Ca_xNb_{5-x}Sn_xO_{15}$ (x = 0.00, 0.01, 0.05, and 0.10), and fitting parameters obtained from Rietveld refinements.

x	a, b (Å)	c (Å)	Volume (Å^3)	R_P (%)	R_{WP} (%)	χ^2
0.00	12.3497(8)	3.8889(3)	593.12(7)	1.92	2.59	1.35
0.01	12.3453(5)	3.8884(8)	592.62(12)	2.74	5.57	2.03
0.05	12.3511(1)	3.8875(7)	593.04(11)	2.22	2.78	1.25
0.10	12.3519(3)	3.8849(5)	592.72(7)	1.46	1.91	1.31

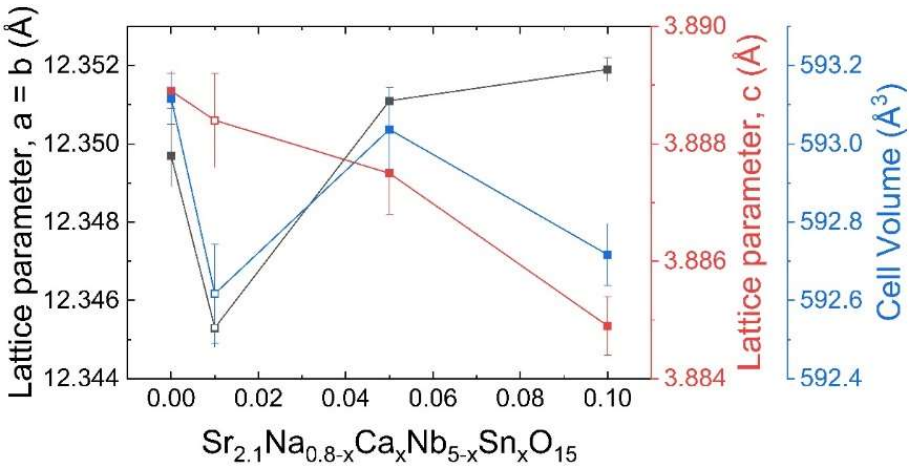

Figure 3 (1.5 column width): Lattice parameters and unit cell volume against composition. Filled symbols represent single phase materials, whereas open symbols represent samples with secondary phase(s).

Backscattered secondary electron images and particle size distribution histograms for all compositions are shown in Figure 4 with unremarkable ceramic microstructure observed for all compositions. Median grain size (d_{50}) varies from ~ 5.1 μm for undoped $Sr_{2.1}Na_{0.8}Nb_5O_{15}$ to ~ 26.6, 23.1 and 6.3 μm for x = 0.01, 0.05, and 0.10, respectively. The differences are most likely related to the difference in sintering temperature between compositions rather than any chemical contributions.

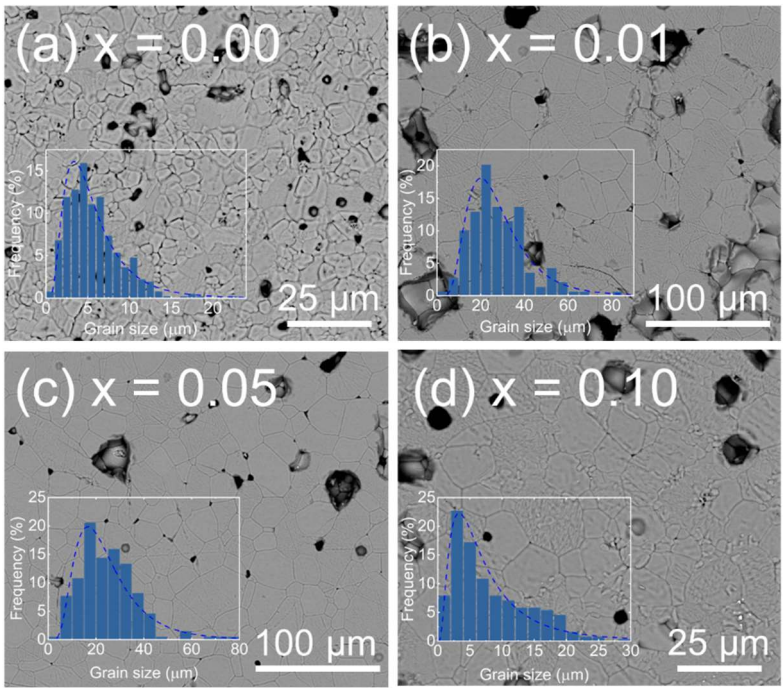

Figure 4 (1.5 column width): Backscattered electron images of polished and thermally etched ceramic surfaces of $Sr_{2.1}Na_{0.8-x}Ca_xNb_{5-x}Sn_xO_{15}$ for (a) x = 0.00, (b) x = 0.01, (c) x = 0.05, and (d) x = 0.10. Insets show grain size distribution for each composition.

The variation in the real part of the relative permittivity (ε') and tan δ with temperature for all compositions at fixed frequencies is shown in Figure 5. For all compositions, two distinct peaks are observed at ~ -25 and ~ 260 °C which are referred to as T1 and T2 respectively, as to be consistent with literature. T2 is attributed to the transition from non-centrosymmetric *P*4*bm* space group to the centrosymmetric *P*4/*mbm* space group, where the second-order Jahn-Teller B-site polarisation is lost and the Nb^{5+} ions are no longer displaced from the centre of the oxygen octahedra. Here, a small level of frequency dispersion can be observed at T2 for x = 0.00, however this may be attributed to space charge contributions as demonstrated in the high temperature region of the tan δ data The behaviour of T1 is more complex with reports of a ferroelectric-ferroelastic transition on cooling with the combination of complex ionic occupancies and a significant number of potential minima for A-site ions to settle generating significant relaxor behaviour [14].

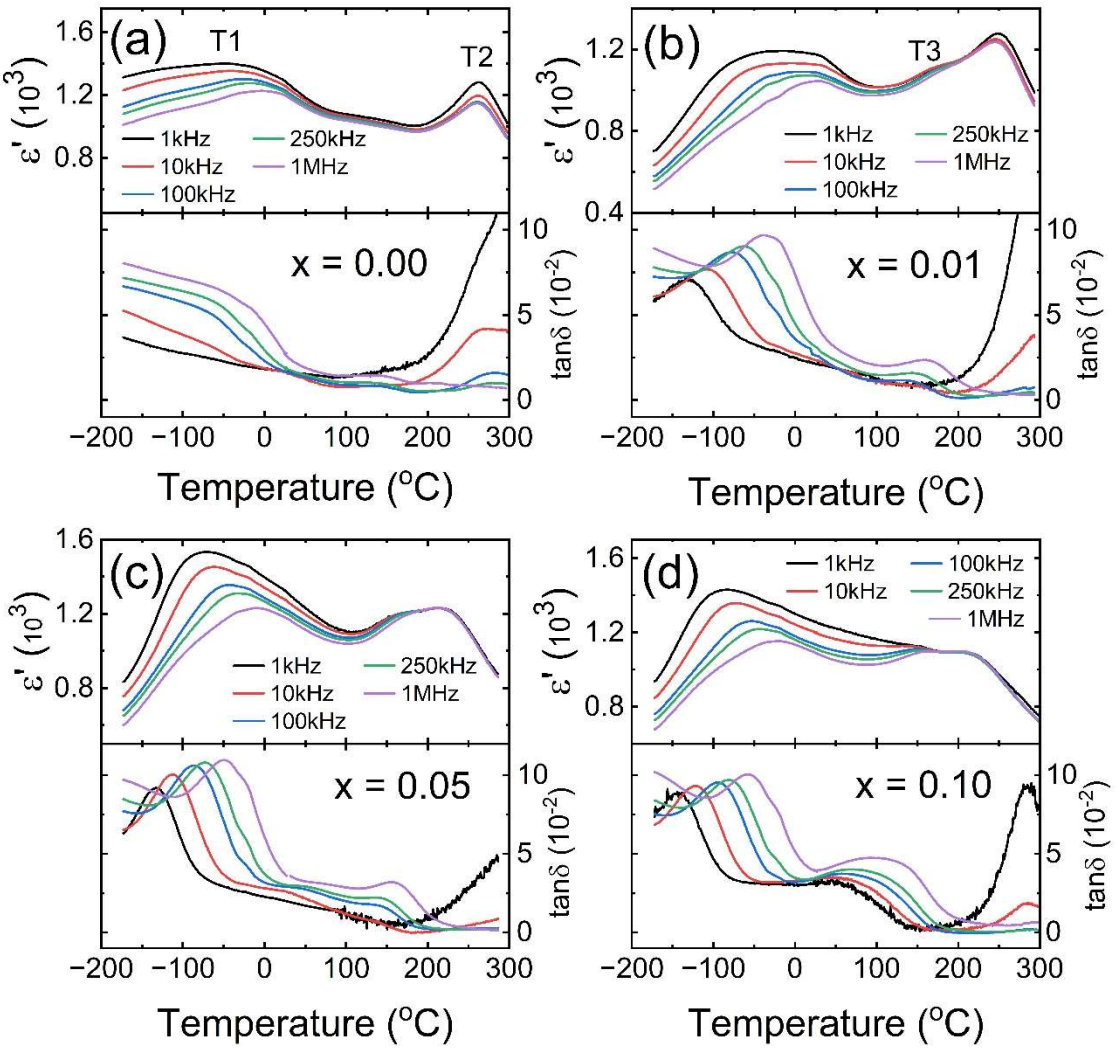

Figure 5 (double column width): Real part of the relative permittivity (ε') and tan δ at fixed frequencies as a function of temperature for (a) x = 0.00, (b) x = 0.01, (c) x = 0.05, and (d) x = 0.10.

Neurgaonkar *et al.* [30] reported orientation dependence in the permittivity response for single crystal SNN. When samples were measured along the [001], two distinct peaks are observed at ~ 100 and 270 °C, whereas the permittivity response along the [110] had a single relaxation with a peak at ~ -95 °C although the nature of these transitions were not discussed thoroughly in this work. Levin *et al.* [6] have proposed that in the TTB structure there are two competing B-sites, B1 and B2. B1 can only polarise along the c-axis; however, B2 has an extra degree of freedom with its polarisation and can rotate between the c-axis and a-b plane. Whilst this hypothesis was constructed within the framework of $(Sr,Ba)Nb_2O_6$, this may be extended to SNN, where the single relaxation observed in the single crystal [110] direction may be the reorientation of the B2-ions from along to the a-b plane to along the c-axis on heating.

As the $CaSnO_3$ concentration increases, a third peak labelled T3 becomes more prevalent in both the ε' and tan δ data. The presence of T3 has been previously mentioned in literature, however with two explanations. The first is space charge behaviour due to excess free charge carriers from Na and/or O loss during processing [18, 19]. The second explanation is a phase transition from the orthorhombically distorted *Im*2*a* or *Cmm*2 space group to the non-centrosymmetric ferroelectric *P*4*bm* space group [35]. Given the nature of tan δ as a function of temperature and frequency within this temperature range as shown in Figure 5, we suggest that T3 is 'real' behaviour associated with a subtle phase transition and therefore the latter explanation is preferable. However as mentioned previously, no evidence of peaks at ~ 9° and/or ~ 17° 2θ (for Mo-Kα source, λ = 0.7096 Å) that signal either the *Im*2*a*, *Cmm*2 or the *Ama*2 structure could not be observed. It is likely that this transition is too subtle to observe with conventional laboratory XRD, and the use of neutron diffraction and/or national facility high energy x-rays are required.

The introduction of $CaSnO_3$ appears to increases the temperature coefficient of capacitance (TCC) compared to undoped SNN0.8. For undoped samples, the high temperature limit in which permittivities exceed ± 15% compared to room temperature values for an R-type capacitor increases from 82 to 120 °C from 1-1000 kHz, significantly lower than current commercial capabilities. For x= 0.10, the dielectric stability increases such that the ±15% window extends from -151 to 225 °C at 1 kHz to -115 to 256 °C at 1 MHz. Although this composition may be useful for potential X9R applications at relatively low frequencies (< 10 kHz), the low temperature transition T1 causes a significant increase in tan δ values which exceed 0.05 at frequencies ≥ 100 kHz, and therefore comply with Y9R and Z9R classifications instead of X9R at higher frequencies.

Curie-Weiss plots for all compositions along with extrapolated Curie temperature (T_0) and Curie-Weiss constant (C_{CW}) are shown in Figure 6. As the $CaSnO_3$ content increases, there is an increase in C_{CW} and a systematic decrease in T_0 as the magnitude of ε' at the high temperature transition T2 decreases. As mentioned previously, this behaviour in TTBs is indicative of the destabilisation of the polar [001] mode associated with the shrinking of the unit cell volume and c-axis lattice parameter. Similar behaviour was observed by Xie and Akimune [24], and again by Yang *et al*. [17], where an increase in concentration of Ca^{2+} in $Sr_{2-x}Ca_xNaNb_5O_{15}$ resulted in the systematic decrease in the magnitude of ε' at T2 until a complete disappearance of this transition at 0.25 < x < 0.35. Although a smaller compositional space is explored in this study, it is likely that this behaviour will follow the same trend at higher $CaSnO_3$ concentrations as the solid solution limit was not observed by XRD. Interestingly, no T3 was observed in the study by Xie and Akimune for any composition.

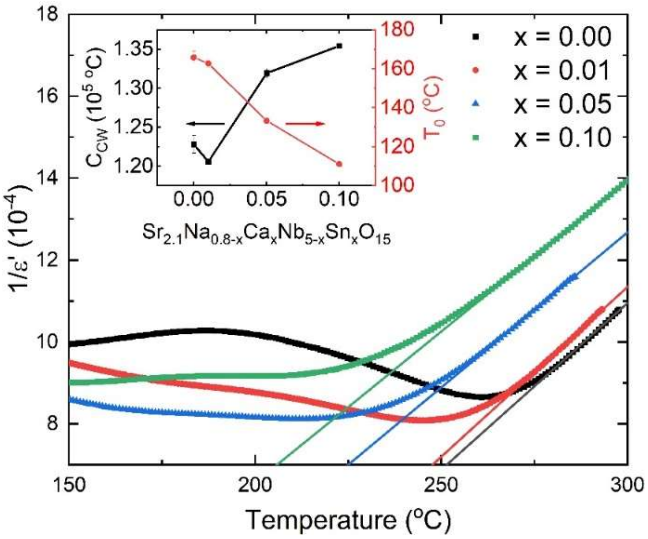

Figure 6 (single column width): Curie-Weiss plots (1/ε' vs T) for all compositions. Inset shows extrapolated Curie-Weiss constant (C_{CW}) and Curie temperature (T_0) against composition.

Spectroscopic plots of the imaginary parts of impedance (Z'') and electric modulus (M'') at ~ 650 °C are shown in Figure 7 and all data could be modelled on an equivalent circuit based on a single, parallel resistor-capacitor, RC element. The agreement in relaxation frequency between the two peaks demonstrates a degree of electrical homogeneity corresponding to a permittivity of ~ 25 pF/cm for all compositions which is consistent with a bulk (paraelectric) response. Furthermore, no increase in the Z'' spectra at low frequency demonstrates predominantly electronic conduction.

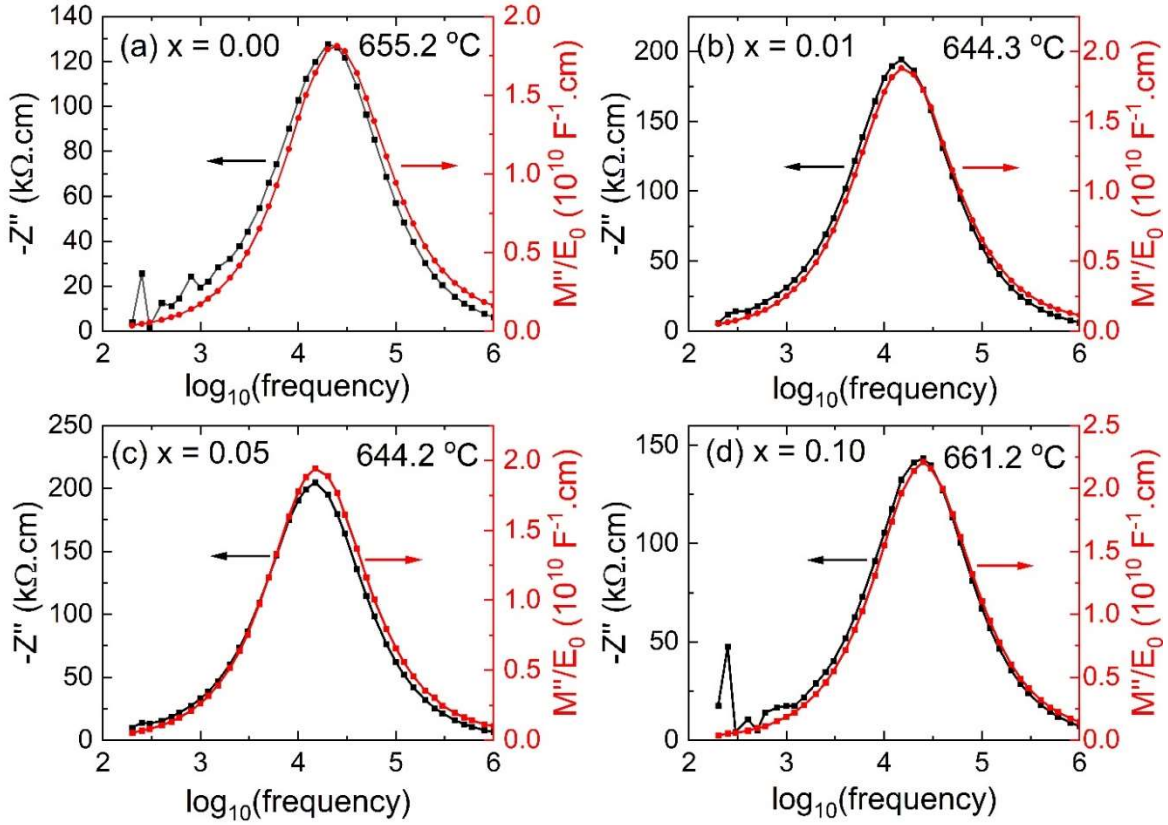

Figure 7 (single column width): Imaginary components of impedance (Z'') and electric modulus (M''/E_0) as a function of $\log_{10}$(frequency) for (a) x = 0.00, (b) x = 0.01, (c) x = 0.05, and (d) x = 0.10

The Arrhenius plot for all compositions is shown in Figure 8. The activation energy increases from ~ 1.27 eV for undoped SNN0.8 to ~ 1.32, 1.33, and 1.38 eV for x = 0.01, 0.05 and 0.10, respectively. Given the magnitude of the activation energy and the temperature range in which these are derived, it is likely that these values represent the intrinsic conduction of these materials and are therefore experimentally derived values for the Fermi energy, and subsequently ~ half the value of the band gap [43].

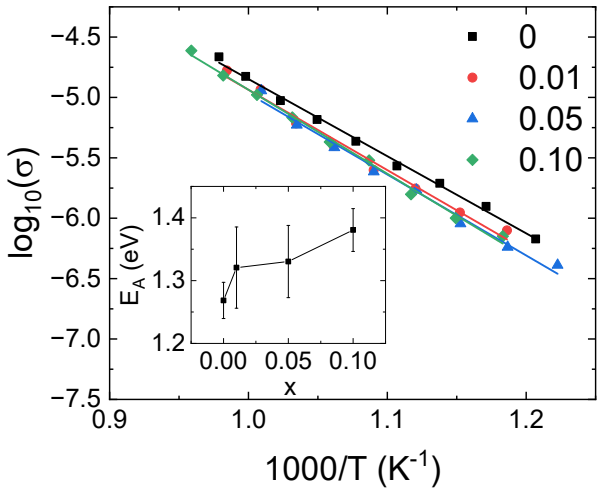

Figure 8 (single column width): Arrhenius plots of conductivity for all compositions. Inset graph shows activation energy (E_A) as a function of composition. Error bars are calculated through propagation of errors associated with line fitting.

4. Conclusions

The structural and dielectric properties of two-stage synthesised $Sr_{2.1}Na_{0.8-x}Ca_xNb_{5-x}Sn_xO_{15}$ (x = 0.00, 0.01, 0.05, 0.10) polycrystalline ceramics have been studied. For single phase samples, the increase in $CaSnO_3$ content results in a decrease in the c-axis lattice parameter and unit cell volume, and an expansion of the a-b plane owing to the introduction of smaller A-site ions and the subsequent reduction of the tolerance factor and tetragonality. With regards to dielectric properties, the Curie temperature T_0 systematically decreases with increasing $CaSnO_3$ content and the appearance of a third transition, T3, becomes more prominent at higher $CaSnO_3$ concentrations. The origin of this dielectric anomaly is currently undetermined as the subtle orthorhombic-tetragonal structural changes that have been suggested in literature are not observed here. Despite variations in microstructure and the presence of secondary phase(s) in x= 0.01 samples, impedance spectroscopy data shows electrical homogeneity in all samples and an increase in the activation energy of intrinsic electronic conduction, signifying the expansion of the band gap with increasing $CaSnO_3$ concentration from ~ 2.54 (x =0.00) to 2.76 eV (x =0.10).

Acknowledgements

The authors would like to thank the Engineering and Physical Sciences Research Council (EPSRC) for financial support (New directions in high temperature dielectrics: unlocking

performance of doped tungsten bronze oxides through mechanistic understanding, EP/V05337X/1).

Author Contributions

Thomas E. Hooper: Data curation, Formal analysis, Methodology, Writing – original draft, Writing – Review and editing

Alexander Crick: Data curation, Formal analysis, Investigation, Methodology

James H. Killeen: Data curation, Formal analysis, Writing – original draft

Derek C. Sinclair: Conceptualization, Supervision, Writing – review & editing

References

[1] P. B. Jamieson, S. C. Abrahams & J. L. Bernstein, Ferroelectric Tungsten Bronze-Type Crystal Structures. I. Barium Strontium Niobate $Ba_{0.27}Sr_{0.75}Nb_2O_{5.78}$. *The Journal of Chemical Physics* **1968,** *48* (11), 5048-5057 10.1063/1.1668176

[2] I. Levin, M. C. Stennett, G. C. Miles, D. I. Woodward, A. R. West & I. M. Reaney, Coupling between octahedral tilting and ferroelectric order in tetragonal tungsten bronze-structured dielectrics. *Applied Physics Letters* **2006,** *89* (122908), 10.1063/1.2355434

[3] J. Gardner & F. D. Morrison, A-site size effect in a family of unfilled ferroelectric tetragonal tungsten bronzes: $Ba_4R_{0.67}Nb_{10}O_{30}$ (R = La, Nd, Sm, Gd, Dy and Y). *Dalton Transactions* **2014,** *43* (30), 11687-95 10.1039/c4dt00126e

[4] A. J. Miller, A. Rotaru, D. C. Arnold & F. D. Morrison, Effect of local A-site strain on dipole stability in $A_6GaNb_9O_{30}$ (A = Ba, Sr, Ca) tetragonal tungsten bronze relaxor dielectrics. *Dalton Transactions* **2015,** *44* (23), 10738-45 10.1039/c4dt03936j

[5] X. Zhu, M. Fu, M. C. Stennett, P. M. Vilarinho, I. Levin, C. A. Randall, J. Gardner, F. D. Morrison & I. M. Reaney, A Crystal-Chemical Framework for Relaxor versus Normal Ferroelectric Behavior in Tetragonal Tungsten Bronzes. *Chemistry of Materials* **2015,** *27* (9), 3250-3261 10.1021/acs.chemmater.5b00072

[6] V. Krayzman, A. Bosak, H. Y. Playford, B. Ravel & I. Levin, Incommensurate Modulation and Competing Ferroelectric/Antiferroelectric Modes in Tetragonal Tungsten Bronzes. *Chemistry of Materials* **2022,** *34* (22), 9989-10002 10.1021/acs.chemmater.2c02367

[7] W. Fortin, G. E. Kugel & D. Rytz, Second harmonic generation (SHG) in $K_6Li_4Nb_{10}O_{30}$(KLN) and effect of non-stoichiometry. *Ferroelectrics* **1997,** *202* (1), 183-191 10.1080/00150199708213475

[8] W. Fortin, G. E. Kugel & D. Rytz, Effects of non-stoichiometry on Raman spectra of $K_6Li_4Nb_{10}O_{30}$ (KLN) compounds. *Ferroelectrics* **1997,** *202* (1), 131-138 10.1080/00150199708213469

[9] K. Li, X. Li Zhu, X. Qiang Liu & X. Ming Chen, Relaxor ferroelectric characteristics of $Ba_5LaTi_3Nb_7O_{30}$ tungsten bronze ceramics. *Applied Physics Letters* **2012,** *100* (1), 012902 10.1063/1.3673913

[10] H.-Y. Lee & R. Freer, High order incommensurate modulations and incommensurate superstructures in transparent $Sr_{0.6}Ba_{0.4}Nb_2O_6$ (SBN40) ceramics. *Journal of Applied Crystallography* **1998,** *31*, 683-691 10.1107/S0021889898003550

[11] C. Li, Y. Zhang, J. Liu & H. A. Graetsch, Long-Range and Local Structure of $Sr_xBa_{1-x}Nb_2O_6$ (x = 0.33 and 0.67) across the Ferroelectric–Relaxor Transition. *Chemistry of Materials* **2020,** *32* (5), 1844-1853 10.1021/acs.chemmater.9b04122

[12] J. R. Oliver, R. R. Neurgaonkar & L. E. Cross, A thermodynamic phenomenology for ferroelectric tungsten bronze $Sr_{0.6}Ba_{0.4}Nb_2O_6$ (SBN:60). *Journal of Applied Physics* **1988,** *64* (1), 37-47 10.1063/1.341438

[13] E. Garcia-Gonzalez, A. Torres-Pardo, R. Jimenez & J. M. Gonzalez-Calbet, Structural singularities in ferroelectric $Sr_2NaNb_5O_{15}$. *Chemistry of Materials* **2007,** *19*, 3575-3580 10.1021/cm071303w

[14] A. Torres-Pardo, R. Jimenez, J. M. Gonzalez-Calbet & E. Garcia-Gonzalez, Structural effects behind the low temperature nonconventional relaxor behavior of the $Sr_2NaNb_5O_{15}$ bronze. *Inorganic Chemistry* **2011,** *50* (23), 12091-8 10.1021/ic2016098

[15] D.-S. Tang, J.-K. Liang, T.-J. Shi, Y.-L. Shang, J.-H. Tian & W.-X. Li, Investigation of the Pseudo-Ternary System $SrNb_2O_6$-$NaNbO_3$-$LiNbO_3$. *Acta Physica Sinica* **1979,** *28* (1), 62-77 10.7498/APS.28.62

[16] S. Xu, P. Yang, Z. Deng, L. Wei & Z. Yang, Effects of Bi substitution on the structures, electrical properties, and transparency of $Sr_2Na_{1-3x}Bi_xNb_5O_{15}$ ceramics. *Materials Research Bulletin* **2020,** *124*, 110774 10.1016/j.materresbull.2020.110774

[17] B. Yang, J. Li, P. Yang, L. Wei & Z. Yang, Effects of A-site cations on the electrical behaviors in $(Sr_{1-x}Ca_x)_{2.1}Na_{0.8}Nb_5O_{15}$ tungsten bronze ferroelectrics. *Materials Chemistry and Physics* **2020,** *243*, 122006 10.1016/j.matchemphys.2019.122006

[18] L. Cao, Y. Yuan, X. Meng, E. Li & B. Tang, Ferroelectric-Relaxor Crossover and Energy Storage Properties in $Sr_2NaNb_5O_{15}$-Based Tungsten Bronze Ceramics. *ACS Applied Materials & Interfaces* **2022,** *14* (7), 9318-9329 10.1021/acsami.1c23673

[19] L. Cao, Y. Yuan, X. Zhang, E. Li & S. Zhang, Relaxor Nature and Energy Storage Properties of $Sr_{2-x}M_xNaNb_{5-x}Ti_xO_{15}$ (M = La^{3+} and Ho^{3+}) Tungsten Bronze Ceramics. *ACS Sustainable Chemistry & Engineering* **2020,** *8* (47), 17527-17539 10.1021/acssuschemeng.0c06861

[20] S. Xu, S. shen, R. Hao, Z. Peng, F. Zhang, D. Wu, P. Liang, X. Chao, L. Wei & Z. Yang, Relaxor nature and superior energy storage performance of $Sr_2Ag_{0.2}Na_{0.8}Nb_5O_{15}$-based tungsten bronze ceramics through B-site substitution. *Chemical Engineering Journal* **2022,** *433*, 133812 10.1016/j.cej.2021.133812

[21] X. Zhang, W. Ye, X. Bu, P. Zheng, L. Li, F. Wen, W. Bai, L. Zheng & Y. Zhang, Remarkable capacitive performance in novel tungsten bronze ceramics. *Dalton Transactions* **2021,** *50* (1), 124-130 10.1039/d0dt03511d

[22] T. Brown, A. P. Brown, D. A. Hall, T. E. Hooper, Y. Li, S. Micklethwaite, Z. Aslam & S. J. Milne, New high temperature dielectrics: Bi-free tungsten bronze ceramics with stable permittivity over a very wide temperature range. *Journal of the European Ceramic Society* **2021,** *41* (6), 3416-3424 10.1016/j.jeurceramsoc.2020.10.034

[23] K. Matsuo, R.-J. Xie, Y. Akimune & T. Sugiyama, Preparation of Lead-Free $Sr_{2-x}Ca_xNaNb_5O_{15}$ (x=0.1)-Based Piezoceramics with Tungsten Bronze Structure. *Journal of the Ceramic Society of Japan* **2002,** *110* (5), 491-494 10.2109/jcersj.110.491

[24] R.-J. Xie & Y. Akimune, Lead-free piezoelectric ceramics in the $(1-x)Sr_2NaNb_5O_{15}$–$(x)Ca_2NaNb_5O_{15}$ ($0.05 \le x \le 0.35$) system. *Journal of Materials Chemistry* **2002,** *12* (10), 3156-3161 10.1039/b202923p

[25] R.-J. Xie, Y. Akimune, R. Wang, N. Hirosaki & T. Nishimura, Dielectric and Piezoelectric Properties of Barium-substituted $Sr_{1.9}Ca_{0.1}NaNb_5O_{15}$Ceramics. *Japanese Journal of Applied Physics* **2003,** *42* (12), 7404-7409 10.1143/jjap.42.7404

[26] R.-J. Xie, Y. Akimune, R. Wang, K. Matsuo, T. Sugiyama & N. Hirosaki, Spark plasma sintering of tungsten bronze $Sr_{2-x}Ca_xNaNb_5O_{15}$ (x=0.1) Piezoelectric Ceramics: I, Processing and Microstructure. *Journal of the American Ceramic Society* **2002,** *85* (11), 2725-2730 10.1111/j.1151-2916.2002.tb00520.x

[27] R.-J. Xie, Y. Akimune, R. Wang, K. Matsuo, T. Sugiyama & N. Hirosaki, Spark plasma sintering of tungsten bronze $Sr_{2-x}Ca_xNaNb_5O_{15}$ (x=0.1) Piezoelectric Ceramics: II, Electrical Properties. *Journal of the American Ceramic Society* **2002,** *85* (11), 2731-2737 10.1111/j.1151-2916.2002.tb00521.x

[28] S. Hao, J. Li, Q. Sung, L. Wei & Z. Yang, Improved electrical properties and good thermal luminescent stability of Sm^{3+} doped $Sr_{1.90}Ca_{0.15}Na_{0.90}Nb_5O_{15}$ multifunctional ceramics. *Journal of Materials Science: Materials in Electronics* **2019,** *30* (14), 13372-13380 10.1007/s10854-019-01704-3

[29] S. Hao, J. Li, P. Yang, L. Wei & Z. Yang, Enhanced electrical properties and strong red light-emitting in Eu^{3+} doped $Sr_{1.90}Ca_{0.15}Na_{0.9}Nb_5O_{15}$ ceramics. *Journal of the American Ceramic Society* **2017,** *100* (12), 5620-5628 10.1111/jace.15085

[30] R. R. Neurgaonkar, W. K. Cory, J. R. Oliver, E. J. Sharp, G. L. Wood, M. M. J., W. W. Clark III & G. J. Salamo, Growth and ferroelectric properties of tungsten bronze $Sr_{2-x}Ca_xNaNb_5O_{15}$ single crystals. *Materials Research Bulletin* **1988,** *23*, 1459-1467 10.1016/0025-5408(88)90272-3

[31] C.-D. Oh, M.-S. Kim, J.-H. Lee, J.-J. Kim, H. Y. Lee & S.-H. Cho, Microstructure evolution and dielectric properties of $(Ba_{1-x}Sr_x)_4Na_2Nb_{10}O_{30}$ ceramics with different Ba/Sr ratios. *Integrated Ferroelectrics* **2006,** *74* (1), 61-70 10.1080/10584580500413889

[32] L. Wei, Z. Yang, R. Gu & H. Pan, Role of structural changes in dielectric, ferroelectric properties of $Sr_2K_xNa_{1-x}Nb_5O_{15}$ lead-free ceramics. *Materials Chemistry and Physics* **2011,** *126* (3), 836-842 10.1016/j.matchemphys.2010.12.032

[33] B. Yang, F. Li, J. P. Han, X. J. Yi, H. L. W. Chan, H. C. Chen & W. Cao, Structural, dielectric and optical properties of barium strontium sodium niobate $(Sr_{0.7}Ba_{0.3})_2NaNb_5O_{15}$ single crystals. *Journal of Physics D: Applied Physics* **2004,** *37* (6), 921-924 10.1088/0022-3727/37/6/017

[34] R. Q. Yin, P. Zheng, J. C. Wang, B. W. Dai, L. M. Zheng, J. Du, L. Zheng, J. X. Deng, K. X. Song & H. B. Qin, Structural and electrical properties of K-doped $Sr_{1.85}Ca_{0.15}NaNb_5O_{15}$ lead-free piezoelectric ceramics. *Ceramics International* **2016,** *42* (8), 10349-10354 10.1016/j.ceramint.2016.03.159

[35] J. Fan, B. Yang, L. Wei & Z. Wang, B-cation effect on relaxor behavior and electric properties in $Sr_2NaNb_{5-x}Sb_xO_{15}$ tungsten bronze ceramics. *Ceramics International* **2016,** *42* (3), 4054-4062 10.1016/j.ceramint.2015.11.077

[36] Y. Dan, X. Zheng, Y. Meng, S. Wu, C. Hu, L. Liu & L. Fang, Simultaneously achieving large energy storage density and high efficiency in the optimized $Sr_2NaNb_5O_{15}$ system with excellent temperature stability at a low electric field. *Ceramics International* **2024,** *50* (4), 6801-6813 10.1016/j.ceramint.2023.12.023

[37] J.-H. Ko, D. H. Kim, S. G. Lushnikov, R. S. Katiyar & S. Kojima, Dielectric Anomalies of $(K_{0.5}\ Na_{0.5})_{0.2}(Sr_{0.75}Ba_{0.25})_{0.9}Nb_2O_6$ Single Crystals with the Tungsten Bronze Structure. *Ferroelectrics* **2011,** *286* (1), 61-71 10.1080/00150190390206239

[38] L. Wei, Z. Yang, X. Han & Z. Li, Structures, dielectric and ferroelectric properties of $Sr_{2-x}Ca_xNaNb_5O_{15}$ lead-free ceramics. *Journal of Materials Research* **2012,** *27* (7), 979-984 10.1557/jmr.2012.32

[39] S. Xu, Z. Deng, S. Shen, L. Wei & Z. Yang, Structural and electrical effects of Ag substitution in tungsten bronze $Sr_2Ag_xNa_{1-x}Nb_5O_{15}$ ceramics. *Ceramics International* **2020,** *46* (9), 13997-14004 10.1016/j.ceramint.2020.02.199

[40] B. H. Toby & R. B. Von Dreele, GSAS-II: the genesis of a modern open-source all purpose crystallography software package. *Journal of Applied Crystallography* **2013,** *46* (2), 544-549 10.1107/s0021889813003531

[41] L. Li, B. Yang, X. Chao, D. Wu, L. Wei & Z. Yang, Effects of preparation method on the microstructure and electrical properties of tungsten bronze structure $Sr_2NaNb_5O_{15}$ ceramics. *Ceramics International* **2019,** *45* (1), 558-565 10.1016/j.ceramint.2018.09.208

[42] R. D. Shannon, Revised Effective Ionic Radii and Systematic Studies of Interatomic Distances In Halides and Chalcogenides. *Acta Crystallographica Section A* **1976,** *A32*, 751-767 10.1107/S0567739476001551

[43] A. Klein, K. Albe, N. Bein, O. Clemens, K. A. Creutz, P. Erhart, M. Frericks, E. Ghorbani, J. P. Hofmann, B. Huang, et al., The Fermi energy as common parameter to describe charge compensation mechanisms: A path to Fermi level engineering of oxide electroceramics. *Journal of Electroceramics* **2023,** *51* (3), 147-177 10.1007/s10832-023-00324-y

Structural and Dielectric Properties of $CaSnO_3$-doped $Sr_{2.1}Na_{0.8}Nb_5O_{15}$ Ceramics: Supplementary Information

Thomas E. Hooper[1], Alexander Crick, James H. Killeen, and Derek C. Sinclair

Department of Materials Science and Engineering, Sir Robert Hadfield Building, University of Sheffield, Mappin Street, Sheffield S1 3JD, UK

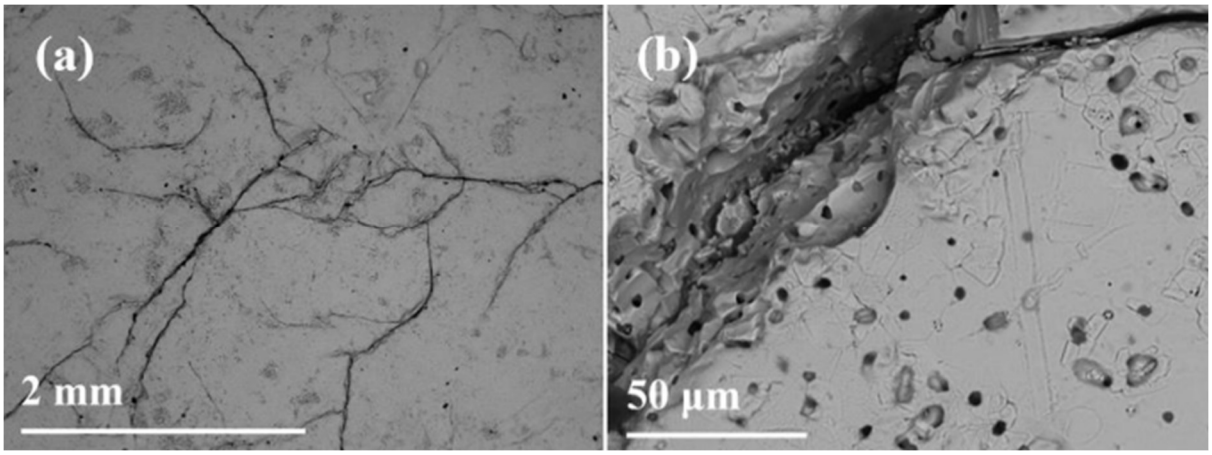

Figure S1: Secondary electron images of polished and etched $Sr_{2.1}Na_{0.8}Nb_5O_{15}$ ceramics sintered at 1350 °C for 5 hours

[1] Corresponding author: thomas.elliot.hooper@gmail.com

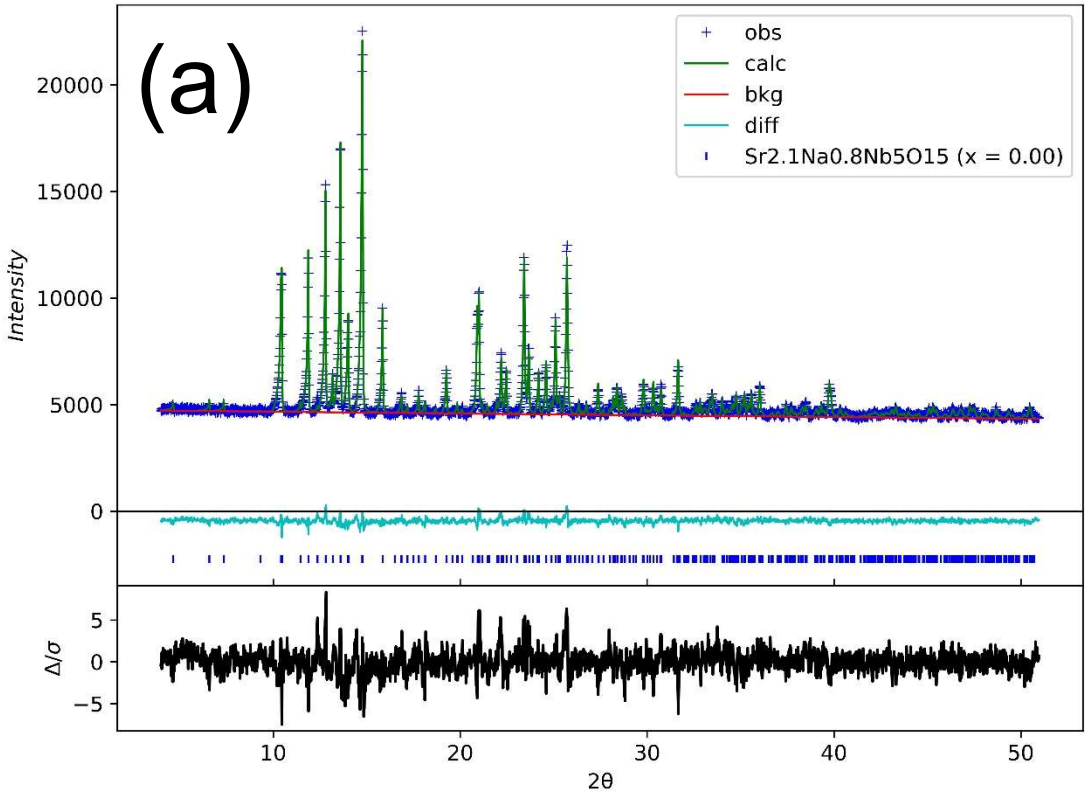
(a)
obs
calc
bkg
diff
Sr2.1Na0.8Nb5O15 (x = 0.00)
Intensity
20000
15000
10000
5000
0
Δ/σ
5
0
−5
10
20
30
40
50
2θ

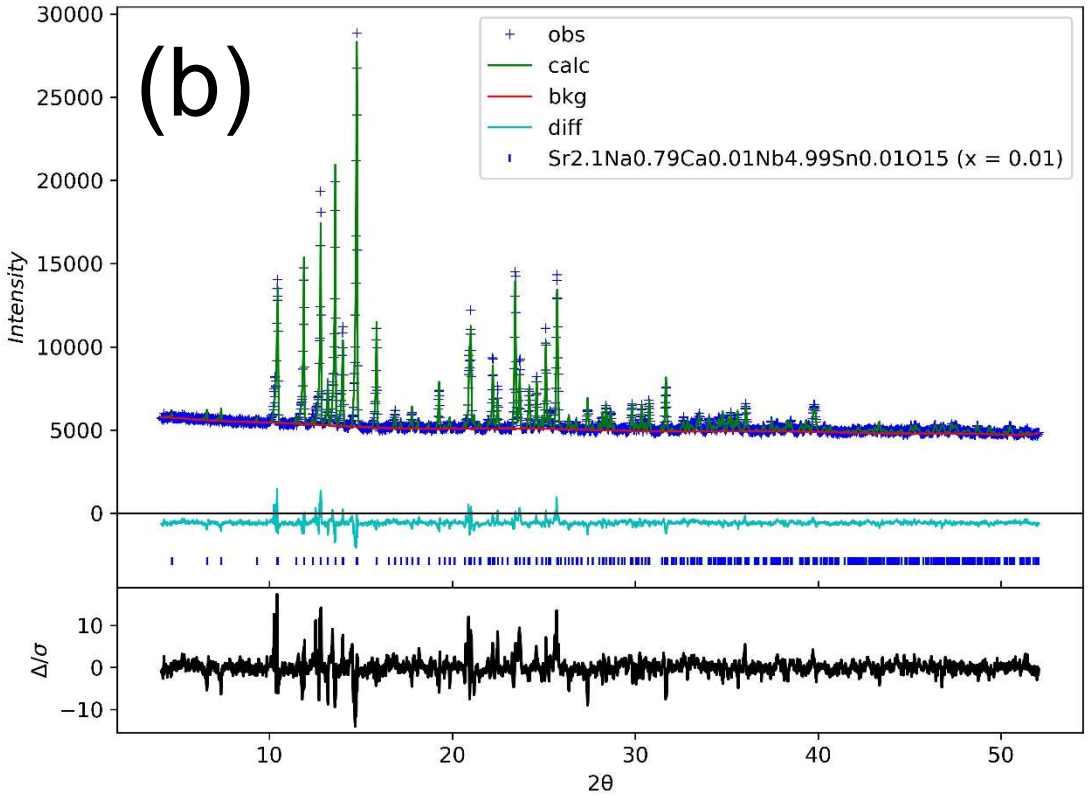
(b)
obs
calc
bkg
diff
Sr2.1Na0.79Ca0.01Nb4.99Sn0.01O15 (x = 0.01)
Intensity
30000
25000
20000
15000
10000
5000
0
Δ/σ
10
0
−10
10
20
30
40
50
2θ

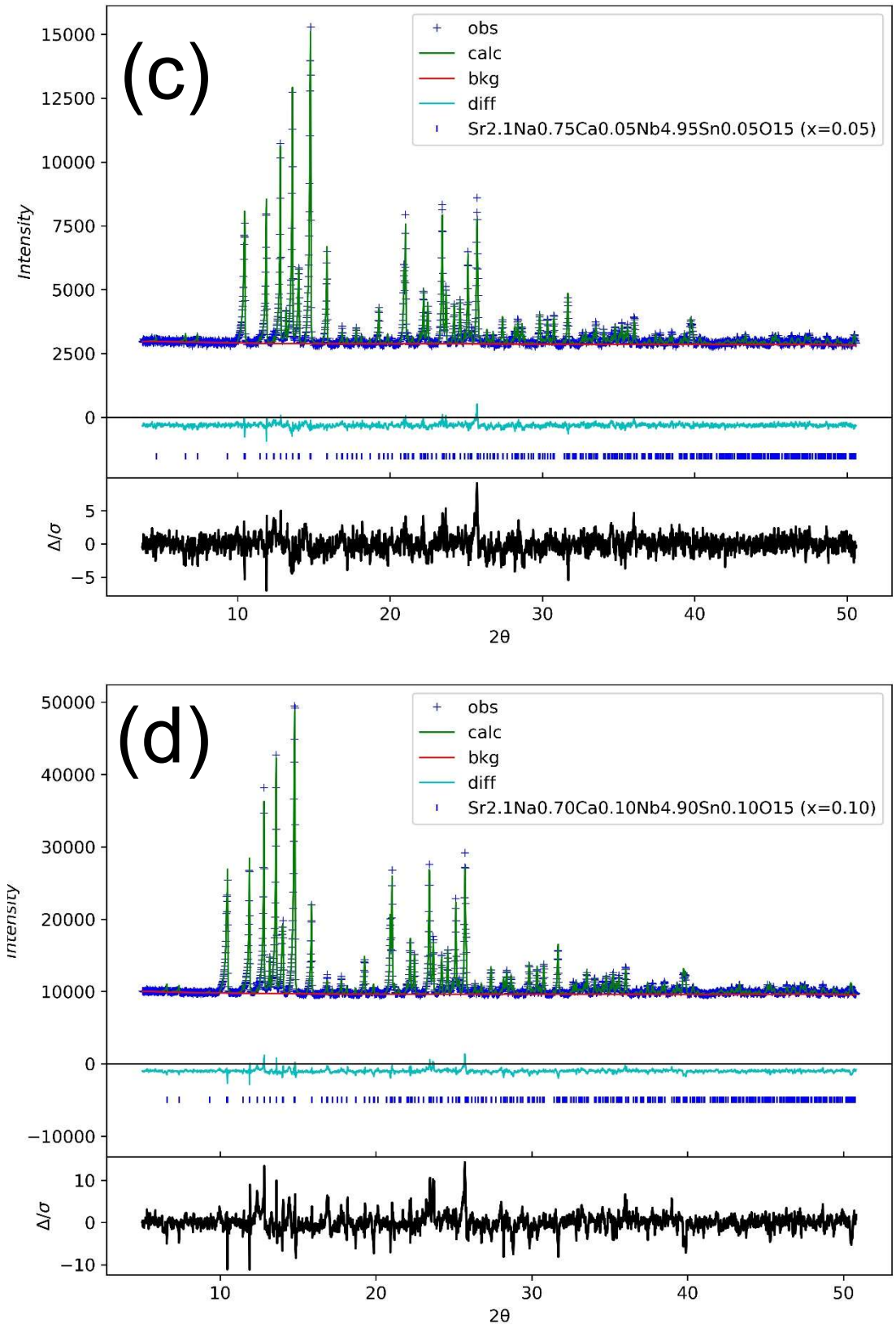

Figure S2: Rietveld refinements for $Sr_{2.1}Na_{0.8-x}Ca_xNb_{5-x}Sn_xO_{15}$ for (a) x = 0.00, (b) x = 0.01, (c) x = 0.05, (d) x = 0.10